Engineering Structures 350 (2026) 121955

Contents lists available at ScienceDirect

Engineering Structures

journal homepage: www.elsevier.com/locate/engstruct

Adaptive NURBS limit analysis coupled with homogenization applied to sail vaults with orthotropy induced by variable brick arrangements

Nicola Grillanda [a], Emanuele Reccia [b,*], Valentina Pintus [b], Antonio Cazzani [b], Gabriele Milani [c,1]

[a] University of Ferrara, DA, Via Quartieri 8, Ferrara 44100, Italy
[b] University of Cagliari, DICAAR, Via Marengo 2, Cagliari 09123, Italy
[c] Politecnico di Milano, ABC, Piazza Leonardo da Vinci 32, Milan 20133, Italy

ARTICLE INFO

Keywords:
Rigid plastic homogenization
Masonry vaults
Adaptive limit analysis
Linear programming
NURBS elements
Settlements

ABSTRACT

It is not uncommon to observe historical masonry vaults which were built with portions where bricks are laid in different preferential alignments, or even where different textures are used. Reasons stand in building technology needs. A stability assessment is a complex task, since irregular orthotropy at the macro-scale is induced by stereotomy, especially in the non-linear range. In presence of double curvature vaults, assessments are carried out by combining limit analysis and finite elements, the latter being needed to correctly reproduce complex crack patterns, which are triggering collapse. This leads to a linear programming problem, which can be similarly used to study the crack propagation in the case of springing settlement. Regardless of the source of degradation, when the vault is built by assembling portions with different textures, this may generate relevant computational issues, such as: analyses need a large number of finite elements, the numerical burden is not affordable and there is a high risk of premature halting. To overcome such problems, the present paper combines, in series, two steps: (i) a homogenization performed in the rigid plastic case with (ii) adaptive NURBS limit analysis. First, a viable homogenization approach, where blocks are assumed to exhibit an infinite compressive resistance and non-linearity is lumped on joints (reduced to interfaces) is proposed, to rapidly deduce homogenized masonry strength domains. Then the vaults are meshed with few NURBS and rigid-plastic spline interfaces, the latter obeying the homogenized failure resistance which was obtained in the first step. Mesh is intentionally rough and progressively adapted in shape to enforce at the converged iteration that some of the NURBS edges coincide with the active cracks, making sure, at the same time, to keep unchanged the edges of contiguous patches with different textures. The proposed methodology–— here applied to a historical sail vault located in Sardinia, Italy — is characterized by a huge improvement in the analysis speed, providing realistic predictions of the load carrying capacity and feasible crack patterns (also in case of settlement), at a fraction of the time needed by heterogeneous approaches.

1. Introduction

Masonry double-curvature structures, which include domes, groins, sails, and cloister vaults, are quite widespread in historical buildings [1, 2]. Their preservation is nowadays considered of major importance, and it depends on the evaluation of their bearing capacity when subjected to both gravitational loads and seismic actions [3–6]. In presence of settlements — which are not uncommon — it is also important to provide predictive information about the expected evolution of the active crack patterns and to estimate the residual resources in terms of applicable overloads [7]. Additionally, when conducting vulnerability assessments at a global scale of entire buildings [5], it is crucial to accurately model vault geometry and correctly determine the structural stiffness and strength [8,9]. These tasks can be quite complex, as the load-bearing capacity and overall stability of historic constructions are heavily influenced by stereotomy [10–12], which refers to the specific arrangement of masonry units. The geometric configuration of the texture impacts the resulting strength of the material at the macro-scale

---

[*] Corresponding author.
E-mail address: emanuele.reccia@unica.it (E. Reccia).

[1] The author Gabriele Milani was an editor of this journal. In accordance with policy, Gabriele Milani was blinded to the entire peer review process

https://doi.org/10.1016/j.engstruct.2025.121955
Received 4 August 2025; Received in revised form 5 November 2025; Accepted 8 December 2025

and hence significantly affects structural performance. Moreover, vaults are specifically designed to support gravity loads based on their geometric shape, adding another layer of complexity [13]. Other common sources of intricacy include the introduction of strengthening elements [14] and the presence of the backfill [15], which is certainly beneficial for gravity loads but may be controversial when horizontal forces– like the seismic ones– are applied.

The structural analysis of single and double-curvature masonry constructions underwent a transformative change following Heyman's foundational work [16–19], leading to the emergence of limit analysis [20,21] (or alternatively constrained min-max problems [22]) as the primary method for assessing their behavior at failure or under settlements. The major advantage of this approach lies in its capacity to accurately replicate mechanisms related to the formation of flexural hinges, where the associated flow rule holds, making it possible to refer to classic upper and lower bound theorems in limit analysis, with an easy association with Finite Elements (FEs) and Distinct Elements (DEs).

An alternative is to refer to the classical funicular approach for masonry arches, assuming that the double curvature vaults are unable to withstand tensile stresses and no sliding is possible, thus generalizing the concept of thrust line in the so-called Thrust Network Analysis, TNA [23–25]. The mechanical rationale of TNA, descending from its relationship with graphical statics, is convincing and is made clear when network nodes are assumed to represent rigid masonry voussoirs, by which a vault can be ideally discretized. This latter approach is undoubtedly fascinating, but presents, in some specific cases, relevant mathematical problems, hardly interfaceable with standard FEs. Moreover, some important features are disregarded with such an approach, like, for instance, the limited frictional resistance, the orthotropy induced by stereotomy and the small tensile strength.

For this reason, it appears more convenient to tackle the problem within standard limit analysis, conveniently coupled with a FE discretization [26].

From a mathematical point of view, any FE limit analysis problem may be always tackled using linear programming (LP), a quite interesting feature if one considers that nowadays there are at disposal many robust commercial software, which are able to deal with problems having thousands of variables, exhibiting outstanding robustness at a very reduced computational burden. Furthermore, LP can be also used to study problems that involve settlements [27], which are probably the main source of concern for historical masonry buildings [28,29].

Within the context of limit analysis, or in case of settlements, the kinematic approach has gained notable attention from the research community due to its user-friendly application [21,26]. This method facilitates both manual analyses through single-variable Lagrangian techniques and more advanced implementations via FEs. While limit analysis has proven effective for assessing collapse mechanisms under lateral loads, existing methodologies often face challenges with geometric irregularities and brick arrangements. A significant gap persists in the automated creation of stereotomy-accurate curved geometries [12] which are suitable for direct application in numerical limit analysis. Such capabilities would not only streamline computational processes but also ensure precise alignment of plastic interfaces with mortar joints, thereby greatly enhancing the accuracy of failure mechanism predictions [11,30].

However, combining limit analysis with a heterogeneous approach that treats individual bricks [30–32] — typically assuming them to be infinitely strong while simplifying the non-linearity of mortar joints to interfaces — can be quite demanding. Even for smaller vaults, the number of masonry units may reach the value of several thousands [33–35]. Using larger blocks, maintaining an unaltered texture and the same height-to-length brick ratios may help in reducing the huge computational burden which is needed, but at the same time it may yield inaccurate results that do not lie on the safe side, as far as the evaluation of the collapse load is concerned. This is a crucial limitation which is exacerbated when blocks are assumed to be infinitely resistant.

An alternative is the use of homogenization [36–38], which is based on the extraction of a representative element of volume (REV) which generates the whole structure by repetition. This method involves solving a boundary value problem on such REV and substituting the assemblage of bricks and mortar at a structural level with a fictitious orthotropic equivalent material, whose mechanical properties are evaluated at the cell level, also known as the meso-scale.

Under the assumption of infinitely resistant bricks and mortar joints reduced to interfaces with rigid-perfectly plastic behavior, limit analysis can be easily combined with homogenization [36–38]. The whole procedure consists of two temporally-separated steps, one where the homogenized strength domain is evaluated at the meso-scale, by repeatedly solving limit analysis problems on the REV, and a second at the macro-scale, where limit analysis is carried out one time on the entire vault, which is assumed to be both homogeneous and orthotropic.

However, whilst attractive in principle, such workflow falls short in terms of computational efficiency, because structural limit analyses computations can be carried out in a manageable manner using a discretization where the elements are infinitely resistant. For instance, when 3D elements are used to mesh a vault, it is possible to assume them dissipating in the bulk, but only for specific classes of materials, and abandoning LP in favor of either Conic Programming (SOCP) or Semi Definite Programming (SDP) [39–41]. Alternatives are possible, e.g. using plate and shell elements, but still the resultant computational burden turns out to compete unfavorably with a direct heterogeneous discretization.

Once accepted the statement that the use, at the macro-scale, of meshes constituted by infinitely resistant elements and by interfaces where all plastic dissipation occurs is necessary, a mesh dependence issue arises. Such an issue can be partially alleviated through refined discretization, although this yields an increase of the computational burden.

Returning to the extra-issues induced by stereotomy, it is not uncommon to observe historical masonry vaults built with portions where bricks are laid in different preferential alignments or, even, where different textures are used. The reasons lie in building technology requirements. A stability assessment becomes, in this case, more complex, since an irregular orthotropy at the macro-scale is introduced.

The present paper is aimed at dealing contemporarily with all such open issues– which are typical of both heterogeneous and homogenized discretization —in a computationally efficient way.

The approach proposed is specifically targeted to solve LP problems within the framework of limit analysis and in presence of foundation settlements, for double curvature masonry vaults which were built by assembling portions of masonry obtained laying bricks according to different textures.

The procedure combines in-series two steps: (i) homogenization performed in the rigid plastic case with (ii) adaptive NURBS limit analysis. First, a viable homogenization approach where blocks are assumed to be infinitely resistant and non-linearity is lumped on joints (simply reduced to interfaces) is proposed, to rapidly deduce homogenized masonry strength domains.

Then, the vault is meshed with few NURBS elements [42], which are assumed to be infinitely resistant and interconnected by rigid-plastic interfaces, equipped with the homogenized strength domain deduced at the meso-scale. NURBS shapes are then progressively modified at the structural level, by means of a meta-heuristic kernel (Genetic Algorithm, GA), enforcing that the element active edges coincide with the actual triggered failure mechanism. The core of the computational approach relies therefore in two separate blocks: (i) derivation of the homogenized strength domain at the meso-scale; and (ii) recursive limit analysis computations at the macro-scale with coarse meshes, where the shape of the elements is progressively adapted by means of a GA. Among the different individuals (meshes), GA selects the ones exhibiting an improved fitness, i.e. a lower collapse multiplier. The procedure, which proved to be extremely fast because of the very unrefined meshes which

Fig. 1. Typical shallow (lowered) sail vaults in Cagliari: simple (a) and paired (b).

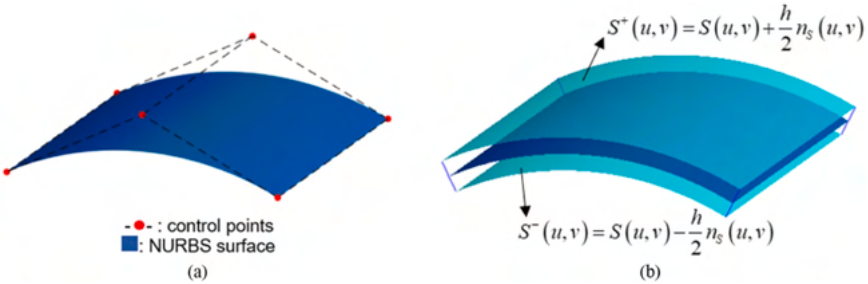

Fig. 2. Definition of a NURBS shell element: (a) NURBS parametric surface representing the middle surface, (b) derived extrados and intrados surfaces.

are used, is benchmarked on a real typology of sail vault — typical of the Sardinian architectural heritage — which exhibits the complication of being built patching the curved surface with bricks disposed in running bond, but with variable orientation from portion to portion, proceeding from the springing to the crown (see Fig. 1). The vault is studied both in the presence of point loads and of springing settlement. A huge improvement in the analysis speed is observed, whereas the obtained results underscore realistic predictions of the load carrying capacity and convincing crack patterns (in case of settlements), at a fraction of the time needed by heterogeneous approaches.

2. Structural level: Adaptive limit analysis with geometry-based orthotropic model

To place more emphasis on the technical applicability of the proposed procedure, first the structural level implementation is concisely discussed hereafter, assuming that the vault is already composed of an orthotropic material. The homogenization model used to derive the mechanical properties of such material will be hence discussed in the subsequent Subsection.

2.1. Characterization of NURBS shell elements

The geometrical description of the adopted shell elements is based on NURBS parametric surfaces, where a NURBS (Non-Uniform Rational B-Spline) derives from the mathematical form of the employed basis functions [43]. In particular, NURBS surfaces are used to represent the middle surface of such shell elements. A NURBS surface is a function **S**: $[0,1]\times[0,1]\rightarrow\mathbb{R}^3$ defined from a mapping of the standard parametric domain (*uv*) to the three-dimensional Euclidean space (*xyz*). Given a spatial net of $(n+1)\times(m+1)$ control points $\mathbf{P}_{ij}$, with associated weights w_{ij}, and two non-uniform knot vectors **u** and **v**, the required rational B-Spline basis functions $R(u, v)$ of degree p and q respectively along the u- and the v-direction are so defined:

$$R_{ij}(u,v)=\frac{N_{i,p}(u)N_{j,q}(v)w_{ij}}{\sum_{k=0}^{n}\sum_{l=0}^{m}N_{k,p}(u)N_{l,q}(v)w_{kl}},\quad i=0,\ldots n; j=0,\ldots m \tag{1}$$

where N are the B-Spline basis functions obtained from the knot vectors through the recursive Cox-De Boor formula [44]. Then, the function representing the NURBS surface is expressed as follows:

$$\mathbf{S}(u,v)=\sum_{i=0}^{n}\sum_{j=0}^{m}R_{ij}(u,v)\mathbf{P}_{ij} \tag{2}$$

It is useful to introduce the two tangential unit vectors $\mathbf{s}_s$ and $\mathbf{t}_s$ and the orthogonal unit vector $\mathbf{n}_s$ for the surface **S**. These can be computed starting from the two partial derivatives of **S** along the u- and the v-direction, here indicated as $\mathbf{S}_u$ and $\mathbf{S}_v$:

$$\begin{aligned}\mathbf{s}_S(u,v)&=\frac{\mathbf{S}_u(u,v)}{||\mathbf{S}_u(u,v)||},\\ \mathbf{t}_S(u,v)&=\frac{\mathbf{S}_v(u,v)}{||\mathbf{S}_v(u,v)||},\\ \mathbf{n}_S(u,v)&=\frac{\mathbf{S}_u(u,v)\times\mathbf{S}_v(u,v)}{||\mathbf{S}_u(u,v)\times\mathbf{S}_v(u,v)||}\end{aligned} \tag{3}$$

In particular, given a thickness value h, $\mathbf{n}_S$ is used to apply an offset transformation and obtain the extrados $\mathbf{S}^{+}$ and intrados $\mathbf{S}^{-}$ surfaces. This operation is needed to convert the middle surface **S** into a shell element, see Fig. 2.

Assemblies of NURBS-based shell elements can be easily used to represent double-curvature structures. Starting from the initial model, a simple mesh can be realized through subdivision of the middle surface of each shell: thanks to the mathematical formulation of NURBS parametric surfaces, such a subdivision can be performed by simply defining a mesh in the parametric domain $[0,1]\times[0,1]$. In this way, the initial NURBS surface is converted into an assembly of trimmed surfaces $\mathbf{S}^{*}$, each one defined within a portion D of the original parametric domain. Then, shells are generated from the trimmed surfaces, see Fig. 3.

Each shell element is treated as a rigid body. The kinematics of the i-th element is described by the six degrees of freedom of its centroid $\mathrm{G_i}$,

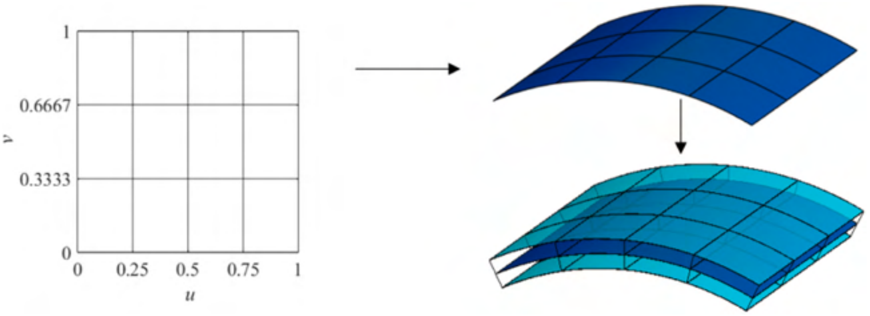

Fig. 3. Example of assembly of NURBS shell elements obtained through a regular mesh defined in the parametric domain.

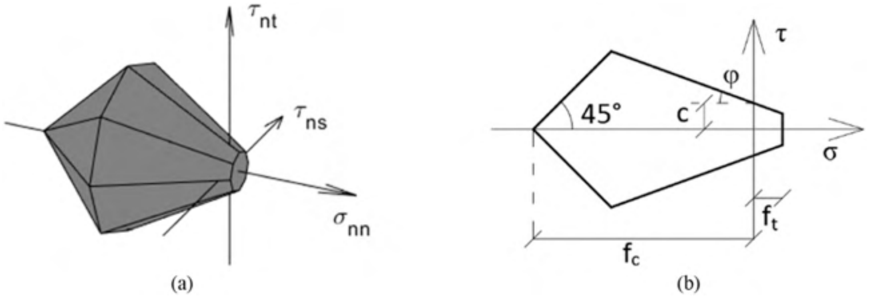

(a)

(b)

Fig. 4. (a) Three-dimensional linearized failure surface and (b) two-dimensional section.

$\dot{\mathbf{u}}_{k,i} = \left[\dot{u}_x, \dot{u}_y, \dot{u}_z, \dot{\phi}_x, \dot{\phi}_y, \dot{\phi}_z\right]_i^T$, where $(\dot{u}_x, \dot{u}_y, \dot{u}_z)$ and $(\dot{\phi}_x, \dot{\phi}_y, \dot{\phi}_z)$ denote, respectively, the three Cartesian components of its translational and rotational velocities defined in the external reference system. Under the hypothesis of small displacements, the kinematics of any other point P belonging to the element is expressed via linearized rigid body kinematics:

$$\dot{\mathbf{u}}_P = \mathbf{A}_G^P \dot{\mathbf{u}}_{k,i}, \text{ in which :}$$
$$\dot{\mathbf{u}}_P = \begin{bmatrix} \dot{u}_{Px} \\ \dot{u}_{Py} \\ \dot{u}_{Pz} \end{bmatrix}, \quad \mathbf{A}_G^P = \begin{bmatrix} 1 & 0 & 0 & 0 & z_P - z_G & y_G - y_P \\ 0 & 1 & 0 & z_G - z_P & 0 & x_P - x_G \\ 0 & 0 & 1 & y_P - y_G & x_G - x_P & 0 \end{bmatrix} \tag{4}$$

Within the kinematic limit analysis tool here applied, this allows to define the power dissipated by the external loads in a linearized way.

2.2. *Geometry-based orthotropic model*

The internal dissipation is supposed to occur only along the contact edges between adjacent elements. Thus, the amount of internal power is evaluated by assuming a rigid-plastic behavior at the interfaces defined on the shell edges. At the same time, the associated flow rule is imposed along the edges through the definition of suitable compatibility constraints. Such constraints can be generally expressed as follows:

$$\Delta\tilde{\dot{\mathbf{u}}} = \dot{\lambda}\frac{\partial f}{\partial \boldsymbol{\sigma}} \tag{5}$$

where: $\Delta\tilde{\dot{\mathbf{u}}}$ is the velocity jump at the interface expressed in the local reference system, $f(\boldsymbol{\sigma})$ is the three-dimensional failure surface defined in the space of local stresses, and $\dot{\lambda}$ are the unknown non-negative plastic multiplier rates. For reader's convenience, let us first discuss the case where the failure surface is isotropic, an assumption that holds in both heterogeneous limit analyses or when the material is assumed unable (or scarcely able) to withstand tensile stresses. In this case, $f(\boldsymbol{\sigma})$ usually consists of a linearized Mohr-Coulomb domain, eventually enriched with tension cut-off and linear cap in compression, see Fig. 4a. The shape of the domain is governed by four constants, which are the tensile f_t and compressive strength f_c, cohesion c, and friction angle φ, as depicted in Fig. 4b. The linearized domain $f(\boldsymbol{\sigma})$ can be written as:

$$f(\boldsymbol{\sigma}) : \ \mathbf{B}\boldsymbol{\sigma} \leq \mathbf{d} \tag{6}$$

where **B** and **d** collect respectively the coefficients and the known terms in the plane equations. Such terms are defined with reference to the resistance parameters (f_t, f_c, c, φ).

From a numerical standpoint, the flow rule along the interface is imposed at a predefined set of points, here indicated as collocation points, located on the interface itself. For a collocation point P on the interface between the i-th and the $i+1$-th elements, the vector of velocity jumps expressed in the local reference system is derived as:

$$\Delta\tilde{\dot{\mathbf{u}}}_P = \mathbf{R}\Delta\dot{\mathbf{u}}_P = \mathbf{R}\left(\mathbf{A}_{Gj+1}^P \dot{\mathbf{u}}_{k,j+1} - \mathbf{A}_{Gj}^P \dot{\mathbf{u}}_{k,j}\right) \tag{7}$$

where $\mathbf{R} = [\mathbf{n}_I, \mathbf{s}_I, \mathbf{t}_I]^T$ contains the normal and the two tangential unit vectors with respect to the interface. By using the properties of NURBS surfaces, it is easy to define the unit vectors in a general form starting from the parametric coordinates. Considering the point $\mathbf{P} = \mathbf{S}(u,v)$ belonging to the interface and the unit vector $\mathbf{r}(u,v) = [r_1(u,v), r_2(u,v)]^T$ which is tangent to the boundary of the parametric domain, the local reference system **R** for the point **P** is evaluated as follows:

$$\mathbf{s}_I(u,v,\mathbf{r}) = \frac{\mathbf{S}_u(u,v)r_1(u,v) + \mathbf{S}_v(u,v)r_2(u,v)}{||\mathbf{S}_u(u,v)r_1(u,v) + \mathbf{S}_v(u,v)r_2(u,v)||} \tag{8}$$

$$\mathbf{t}_I(u,v) = \mathbf{n}_S(u,v) \tag{9}$$

$$\mathbf{n}_I(u,v,\mathbf{r}) = \mathbf{t}_I(u,v,\mathbf{r}) \times \mathbf{s}_I(u,v,\mathbf{r}) + \mathbf{t}_I(u,v)\left(\mathbf{t}_I^T(u,v)\mathbf{s}_I(u,v,\mathbf{r})\right) \tag{10}$$

Note that $\mathbf{t}_I$ is the only unit vector that does not depend on **r**.

For an orthotropic failure surface, little modifications are needed. Indeed, since a perfectly plastic behavior is assumed at the interfaces, the distinction between isotropic and orthotropic behavior stands only in the definition of the ultimate resistance parameters. If the material is isotropic, the same values of resistance parameters are assigned, whatever is the orientation of the normal vector $\mathbf{n}_I$: in other words, the failure surface does not depend on $\mathbf{n}_I$. An orthotropic behavior can be assigned

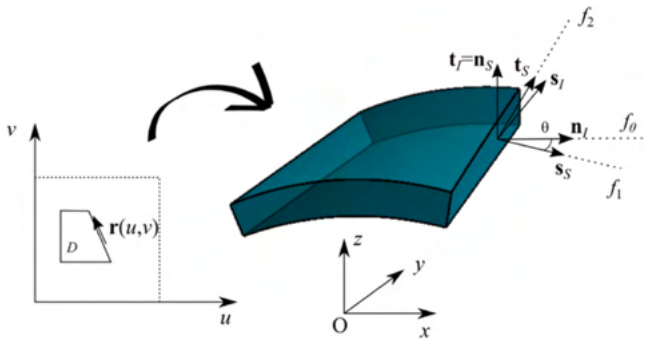

Fig. 5. Local reference system at the interface and orthotropic model.

by considering a Mohr-Coulomb failure surface that is affected by $\mathbf{n}_I$. Let us define θ as the angle between the interface normal vector $\mathbf{n}_I$ and the main texture direction $\mathbf{s}_S$, which is computed as $\theta = \arccos(\mathbf{n}_I^T\mathbf{s}_S)$. This angle characterizes the orientation of the interface relative to the orthotropic material axes and is used to determine the direction-dependent strength parameters. It is now easy to identify the two angles $\theta = \theta_1$ and $\theta = \theta_2$ that correspond respectively to the cases $\mathbf{n}_I\ //\mathbf{S}_u$ and $\mathbf{n}_I\ //\mathbf{S}_v$. The values θ_1 and θ_2 depend on the parametrization of the surface, since $\mathbf{s}_S$ and $\mathbf{t}_S$ are not orthogonal in the general case, meaning that the local reference system identified by Eq. (3) is not orthogonal for all parametric surfaces. However, in the frequent case of partial derivatives orthogonal to each other, we have that $\theta_1 = 0$ and $\theta_2 = \pi/2$. These can be considered as the two main directions for the shell elements, identified with reference to its middle NURBS surface. Two failure surfaces can be defined along the two main directions, namely $f_1(\boldsymbol{\sigma}) = f_{\theta=\theta 1}(\boldsymbol{\sigma})$ and $f_2(\boldsymbol{\sigma}) = f(\boldsymbol{\sigma})_{\theta=\theta 2}$. Then, a function can be assigned to obtain $f_\theta(\boldsymbol{\sigma})$ for any orientation. In the case of orthogonal local reference, Eq. (3), a function typically available in commercial finite element software is the following:

$$f_\theta(\boldsymbol{\sigma}) = f_1(\boldsymbol{\sigma})\cos^2\theta + f_2(\boldsymbol{\sigma})\sin^2\theta \tag{11}$$

which becomes:

$$f_\theta(\boldsymbol{\sigma}):\ \ (\mathbf{B}_1\cos^2\theta + \mathbf{B}_2\sin^2\theta)\boldsymbol{\sigma} \le \mathbf{d}_1\cos^2\theta + \mathbf{d}_2\sin^2\theta \tag{12}$$

It consists of a simple linear interpolation based on quadratic trigonometric functions. However, such a relation generates an overestimation of the resistance values along the intermediate directions, in particular for materials presenting a strongly orthotropic behavior like running bond masonry. Therefore, an elliptical interpolation is adopted here. Since such a relation is non-linear, it must be applied to each individual plane inequality coefficient. We can write:

$$f_\theta(\boldsymbol{\sigma}):\ \mathbf{B}_\theta\boldsymbol{\sigma} \le \mathbf{d}_\theta \tag{13}$$

in which the components $B_{\theta,ij}$ and $d_{\theta,i}$ within matrix $\mathbf{B}_\theta$ and vector $\mathbf{d}_\theta$ (i and j denote rows and columns in $\mathbf{B}_\theta$ and $\mathbf{d}_\theta$) are obtained as:

$$B_{\theta,ij} = \frac{B_{1,ij}B_{2,ij}}{\sqrt{B_{2,ij}^2\cos^2\theta + B_{1,ij}^2\sin^2\theta}}, \qquad d_{\theta,i} = \frac{d_{1,i}d_{2,i}}{\sqrt{d_{2,i}^2\cos^2\theta + d_{1,i}^2\sin^2\theta}} \tag{14}$$

For sake of completeness, we also report here the most general rule corresponding to the case of non-orthogonal local reference:

$$\begin{aligned} B_{\theta,ij} &= \frac{B_{1,ij}B_{2,ij}}{\sqrt{B_{2,ij}^2\cos^2\left(\frac{\pi\theta}{2\theta_2}\right) + B_{1,ij}^2\sin^2\left(\frac{\pi\theta}{2\theta_2}\right)}}, \\ d_{\theta,i} &= \frac{d_{1,i}d_{2,i}}{\sqrt{d_{2,i}^2\cos^2\left(\frac{\pi\theta}{2\theta_2}\right) + d_{1,i}^2\sin^2\left(\frac{\pi\theta}{2\theta_2}\right)}} \end{aligned} \tag{15}$$

in which $\theta_2 = \arccos(\mathbf{s}_S{}^T\mathbf{t}_S)$. A representative schematization of the adopted symbols is reported in Fig. 5. It is easy to observe that, once the expressions for $f_1(\boldsymbol{\sigma})$ and $f_2(\boldsymbol{\sigma})$ are known, Eqs (14)-(15) are based on geometrical quantities only. Therefore, a detailed calibration of the resistance values along the two main directions is fundamental. This study is described in Section 3.

2.3. Principle of virtual powers and mesh adaptation strategy

Once a load configuration $\mathbf{Q}$, which is composed of permanent $\mathbf{Q}_0$ and variable loads $\Gamma\mathbf{Q}_1$ (these latter depending on a load multiplier Γ) has been defined, a simple kinematic limit analysis problem can be written. The powers associated with external loads are easily evaluated by multiplying the resultant of each load for the velocity of the loaded point:

$$\begin{aligned} P_{ext} &= P_{ext,0} + P_{ext,\Gamma} = P_{ext,0} + \Gamma P_{ext,1} = \\ &= \sum\nolimits_{j0}\mathbf{Q}_{0,j0}^T\dot{\mathbf{u}}_{P,j0} + \Gamma\sum\nolimits_{j1}\mathbf{Q}_{1,j1}^T\dot{\mathbf{u}}_{P,j1} \end{aligned} \tag{16}$$

where the quantity $P_{ext,1}$ associated to $\mathbf{Q}_1$ is imposed to have a unit value, in agreement with the standard upper bound limit analysis formulation. In parallel, the power associated with internal stress is defined as the integral of the stress times the velocity jumps along interfaces and, within the assumption of rigid plastic behavior, can be written in terms of linear combination of the plastic multiplier rates:

$$P_{in} = \sum_{h=1}^{N_{\text{int}}}\int_{A_h}\boldsymbol{\sigma}^T\Delta\widetilde{\dot{\mathbf{u}}}\,dA_h = \sum_{h=1}^{N_{\text{int}}}\int_{A_h}\boldsymbol{\sigma}^T\dot{\lambda}\frac{\partial f}{\partial\boldsymbol{\sigma}}dA_h = \sum_{h=1}^{N_{\text{int}}}\left(\sum_{e=1}^{Np}a_e\dot{\boldsymbol{\lambda}}_e^T\mathbf{d}_e\right) \tag{17}$$

where N_{int} is the total number of interfaces, Np is the number of collocation points for each interface, and for the e-th point a_e is the associated area, $\dot{\boldsymbol{\lambda}}_e$ is the vector of unknown plastic multiplier rates and $\mathbf{d}_e$ is the vector of known terms in the plane equations used to linearize the failure surface at that point (note that the failure surface may assume different shapes for each collocation point in the adopted orthotropic model).

By applying the Principle of Virtual Powers, it is possible to write the kinematic load multiplier Γ as a linear combination of the unknowns:

$$\begin{aligned} &P_{in} = P_{ext}\Rightarrow \\ &\Rightarrow\Gamma = \frac{P_{in} - P_{ext,0}}{P_{ext,1}} = \sum_{h=1}^{N_{\text{int}}}\left(\sum_{e=1}^{Np}a_e\dot{\boldsymbol{\lambda}}_e^T\mathbf{d}_e\right) - \sum\nolimits_{j0}\mathbf{Q}_{0,j0}^T\dot{\mathbf{u}}_{P,j0} = \mathbf{c}^T\begin{bmatrix}\dot{\mathbf{u}}\\ \dot{\boldsymbol{\lambda}}\end{bmatrix} \end{aligned} \tag{18}$$

where the global vector of unknowns $[\dot{\mathbf{u}},\dot{\boldsymbol{\lambda}}]^T$ represents a possible mechanism. Without going too much in detail about the kinematic formulation (the interested reader can be referred to [42,45]), $[\dot{\mathbf{u}},\dot{\boldsymbol{\lambda}}]^T$ and Γ can be obtained by applying the Principle of Virtual Powers once geometric and compatibility constraints, and normalization conditions have been enforced.

The following linear programming (LP) problem is written:

$$\min\Gamma = \mathbf{c}^T\begin{bmatrix}\dot{\mathbf{u}}\\ \dot{\boldsymbol{\lambda}}\end{bmatrix}\text{such that}\begin{cases}\mathbf{A}_{geom}\dot{\mathbf{u}} = \mathbf{0}\\ \mathbf{A}_{comp}\left[\dot{\mathbf{u}},\dot{\boldsymbol{\lambda}}\right]^T = \mathbf{0}\\ \sum\nolimits_{j1}\mathbf{Q}_{1,j1}^T\dot{\mathbf{u}}_{P,j1} = 1\\ \dot{\boldsymbol{\lambda}} \ge \mathbf{0}\end{cases} \tag{19}$$

in which $\mathbf{A}_{geom}$ and $\mathbf{A}_{comp}$ represent the geometric and compatibility constraints written in matrix form. Therefore, Eq. (19) allows to find the load-bearing capacity and the mechanism associated with the given load configuration and the adopted mesh.

With slight modifications of Eq. (19) — for further details the reader is referred to [27] — it is possible to write an analogous LP problem aimed at determining the mechanism deriving from an imposed displacement at the external boundary of the structure, the latter

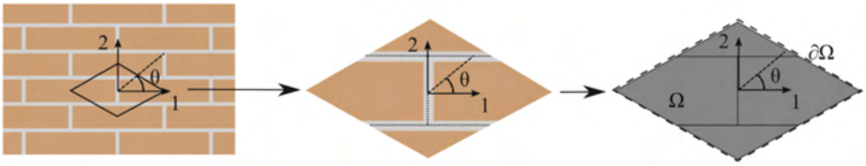

Fig. 6. Definition of the representative element of volume (REV).

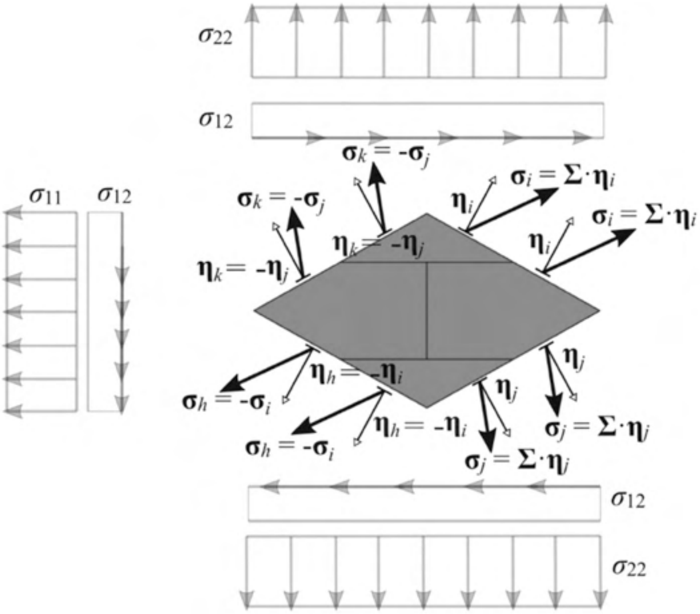

Fig. 7. Stress configuration scheme for the REV from a given stress tensor **Σ**.

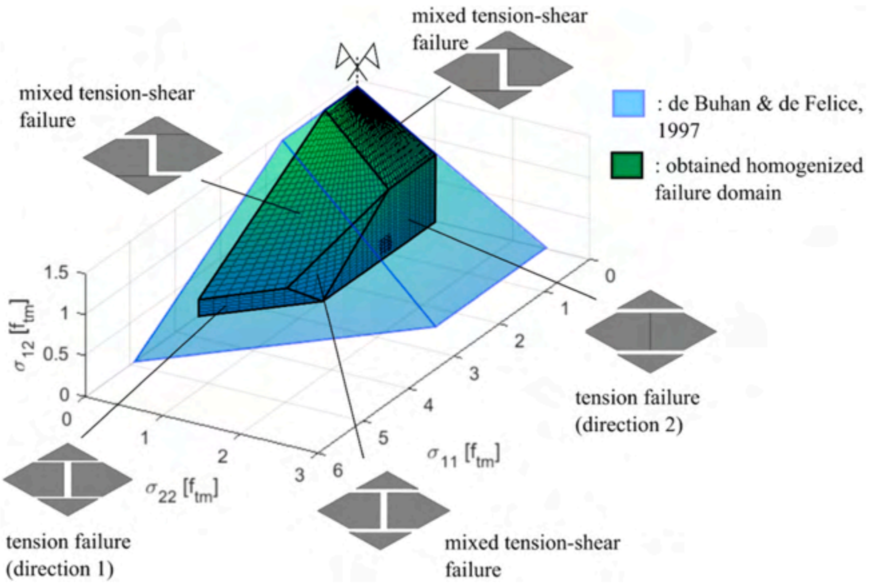

Fig. 8. Derived three-dimensional homogenized failure surface with corresponding failure modes observed on the REV, and comparison with the homogenized failure surface obtained by de Buhan and de Felice [36].

subjected now to permanent loads only. Such a problem requires that the imposed displacement is small with respect to the overall dimension of the model: this assumption is needed not only to maintain a linearized kinematics but also to conceptually express the same constraints by using displacements and plastic multipliers as unknowns, instead of velocities and plastic multiplier rates. In this case, the unit live load power constraint is substituted by imposing the known displacement at the boundary, and, without additional modification, the value of the objective function coincides with the work of the reaction force times the imposed displacement. Such a formulation is useful to determine the structural response to a differential base settlement. Even in this case, reference is made to [27] for a detailed discussion.

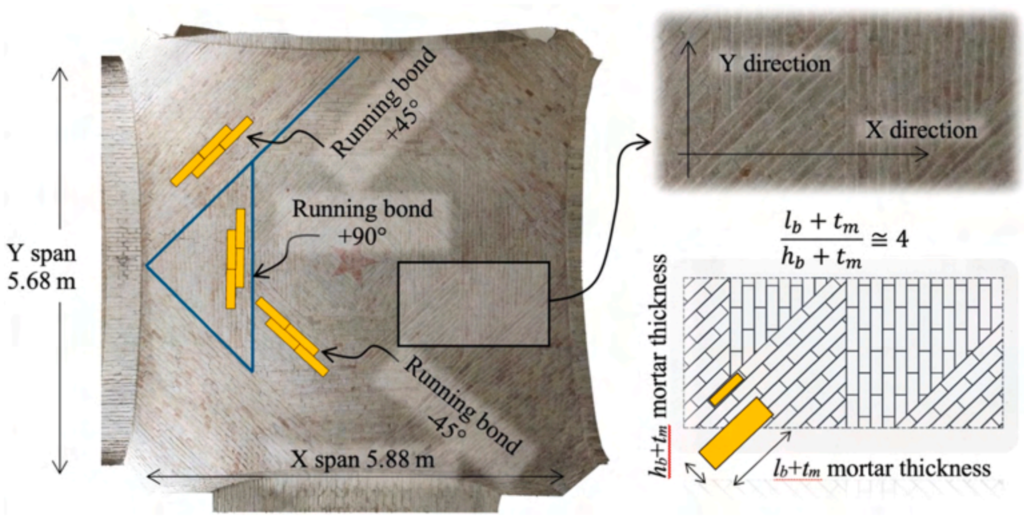

Fig. 9. Result of the photogrammetric survey with texture identification.

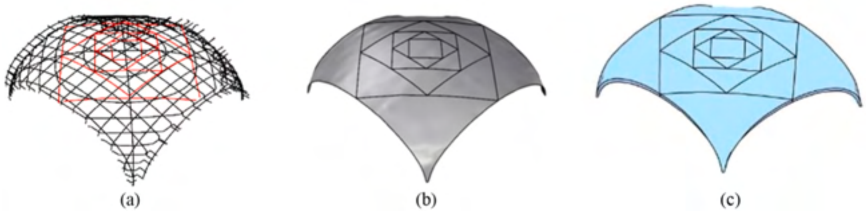

Fig. 10. Construction of the NURBS model of the single vault: (a) section lines, (b) assembly of NURBS surfaces in Rhinoceros and (c) obtained NURBS model in MATLAB.

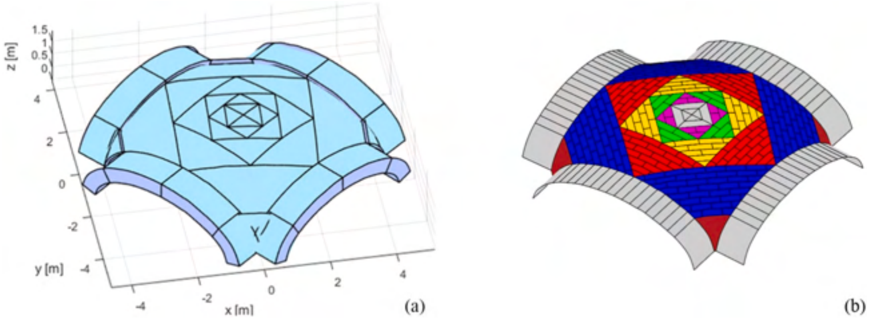

Fig. 11. Sail vault: (a) initial model, (b) qualitative texture representation for each triangular portion.

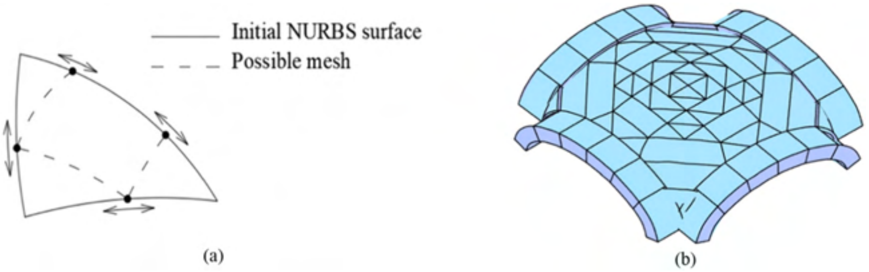

Fig. 12. Definition of a possible mesh: (a) schematization of the mesh for the NURBS surfaces composing the vaults, (b) regular mesh obtained by setting $t_i = 0.5$ for all the lines.

In both problems, the results obtained are strictly related to the initial mesh. Indeed, by considering rigid elements with rigid plastic behavior only at interfaces, the solutions mainly consist of mutual roto-translation along element edges. According to the kinematic theorem of limit analysis, if the position of fracture lines is fixed the obtained load multiplier Γ is an upper bound of the collapse multiplier. It is therefore

Fig. 13. Orthotropic model for masonry: definition of the two main directions (a) on the NURBS surface and (b) with reference to the masonry texture.

Table 1
Material properties adopted for masonry.

Property	Symbol	Value
Specific weight [kN/m^3]	γ	18
Ultimate tensile strength along direction 1[MPa]	f_{t1}	0.18
Ultimate tensile strength along direction 2 [MPa]	f_{t2}	0.05
Ultimate compression strength [MPa]	$f_{c1} = f_{c2}$	1
Cohesion along direction [MPa]	$c_1 = c_2$	1.4 f_{t2}
Friction angle [°]	$\varphi_1 = \varphi_2$	30

required to find the mesh associated with the global minimum value of Γ. A mesh adaptation strategy based on a meta-heuristic algorithm, here a Genetic Algorithm (GA) [46] is used to this aim. Eq. (18) represents the objective function for the GA. The initially regular mesh (Fig. 3), defined within the parametric domain, is iteratively modified by changing the position and the inclination of the internal lines, allowing to obtain curved shell-elements of different shapes which represent the macro-blocks involved in the collapse. At the end of the procedure, the meta-heuristic mesh adaptation allows to find the position of fracture lines associated with the global minimum of Γ, i.e. with the collapse load multiplier.

3. Derivation of the homogenized failure surface

The first step of the procedure, as already pointed out, requires the evaluation of the homogenized strength domain, which, in turn, allows to deduce the ultimate properties of the interfaces. A simple investigation is here conducted in order to have a consistent definition of the resistance parameters $(f_t, f_c, c, \varphi)_\theta$ along a certain direction θ of the interface, which, again, depends on those evaluated along two reference directions. These two main directions, here identified through subscripts 1 and 2, denote respectively the bed joint and the head joint directions, see Fig. 6. According to the hypotheses that will be soon exposed, the tensile strength is the resistance parameter that is affected by the direction along which the material is analyzed.

It must be specified that this study remains focused on the in-plane failure properties of the running bond masonry texture, whereas the out-of-plane properties are uncoupled by the in-plane ones. Therefore, the homogenized failure surface is here defined in the three-dimensional space of stress $(\sigma_{11}, \sigma_{22}, \sigma_{12})$ with reference to the case where the normal stresses σ_{11} and σ_{22} are positive. In other words, since the behavior of the homogenized material remains the same for positive or negative tangential stress σ_{12}, the homogenized failure surface will be defined for the first octant of the three-dimensional stress space $(\sigma_{11}, \sigma_{22}, \sigma_{12} \geq 0)$. A representative element of volume (REV) is studied under plane stress conditions, in particular by considering a stress configuration directed along different orientations. The REV has been defined by considering the textures observed in the sail vaults: such textures are piecewise variable across the vault but correspond to the running bond texture within each partition (see again Fig. 1). Therefore, the REV here considered is composed of four adjacent bricks in agreement with the standard reference volumes adopted for the running bond texture [36], see Fig. 6. Bricks are assumed to be rigid and infinitely resistant, whereas mortar joints are reduced to zero-thickness interfaces. The failure along the interfaces is still governed by a Mohr-Coulomb friction criterion with cap in compression and a tension cut-off: we can thus define the corresponding failure surface $f_m(\boldsymbol{\sigma})$ via Eq. (6) starting from the mortar resistance parameters $(f_t, f_c, c, \varphi)_m$. This denotes a first difference with respect to [36], where the failure along interfaces was described as a purely frictional behavior governed by cohesion and friction angle only. In terms of tension stress, this means that a value f_{tm}, which is lower than $c_m/\tan(\varphi_m)$ is here adopted. With such assumptions, it is expected that the failure of the homogenized material in shear and tension consists of a more complex damage pattern, composed of both tensile failure and sliding phenomena developing along the joints, which will be associated to a homogenized failure surface exhibiting a higher number of constituent planes with respect to the outcome of [36]. With reference to failures in compression, a proper evaluation of the homogenized properties should include the failure (crushing) of bricks in the computation, but at present this issue has been postponed, and the mortar crushing resistance is instead used.

The homogenized failure surface is here identified in a fully numerical way: limit analysis is applied to the REV once a suitable load

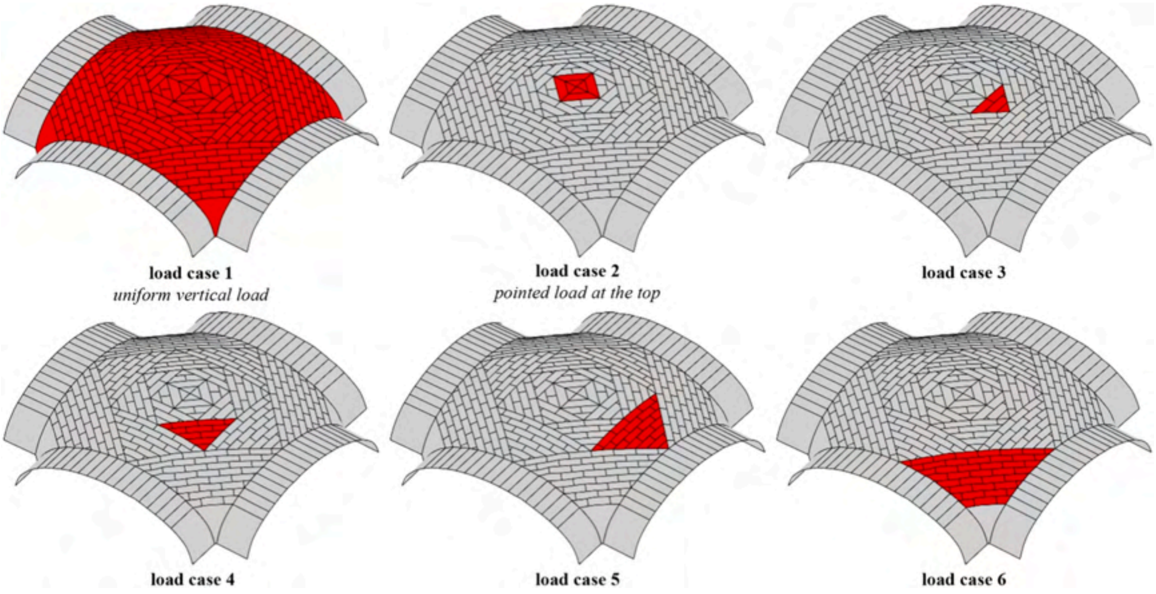

Fig. 14. Different uniform vertical load configurations: loaded area in red.

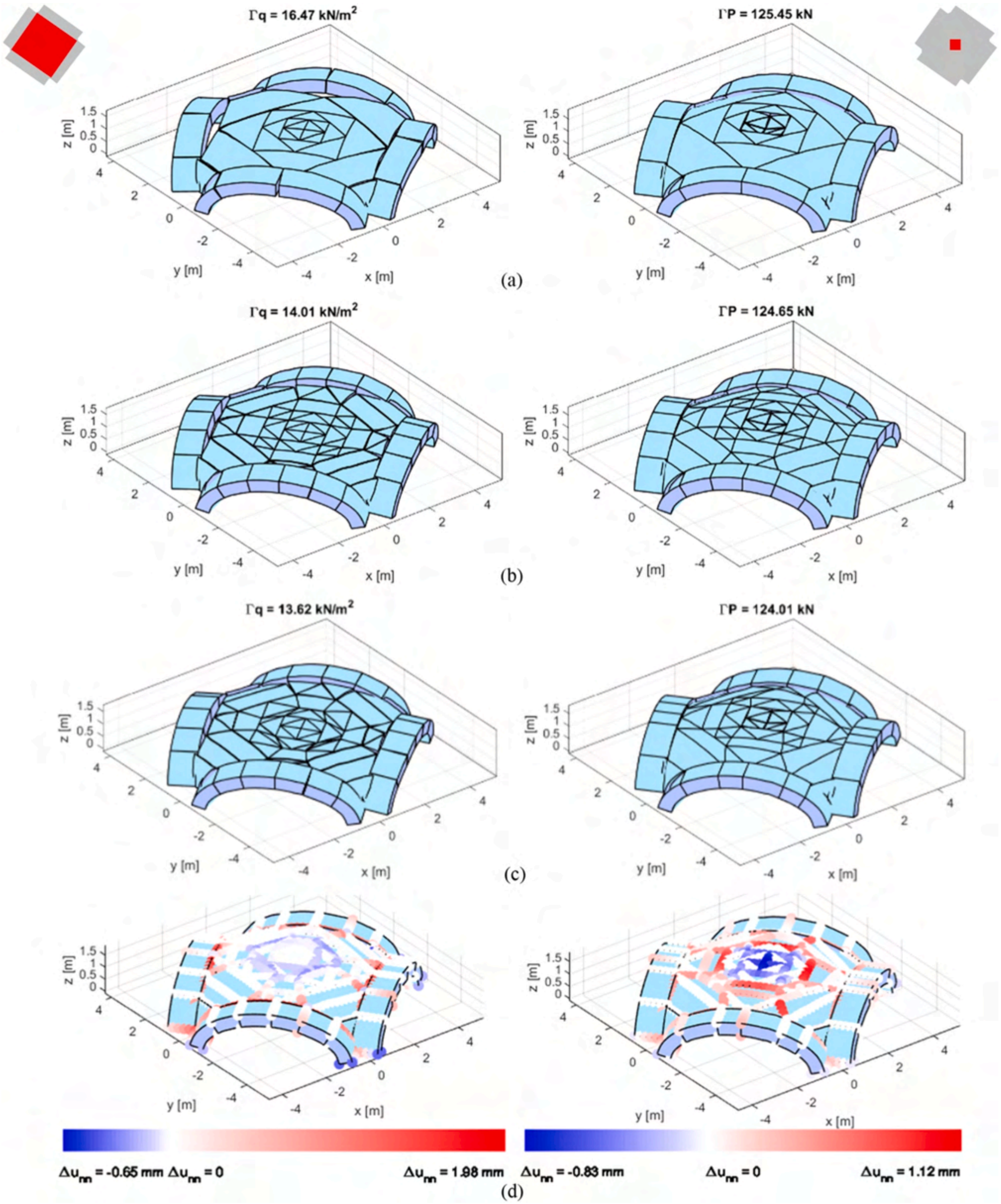

Fig. 15. Sail vault under Load case 1, uniform vertical load (left), and Load case 2, pointed load at the top (right): (a-c) load-bearing capacity and collapse mechanisms in case of no mesh, initial and optimized mesh, (d) colormap representing the normal displacement jumps Δu_{nn} obtained by multiplying the velocity field by a unitary time factor (open crack lines in red, compression failures in blue, no damage in white).

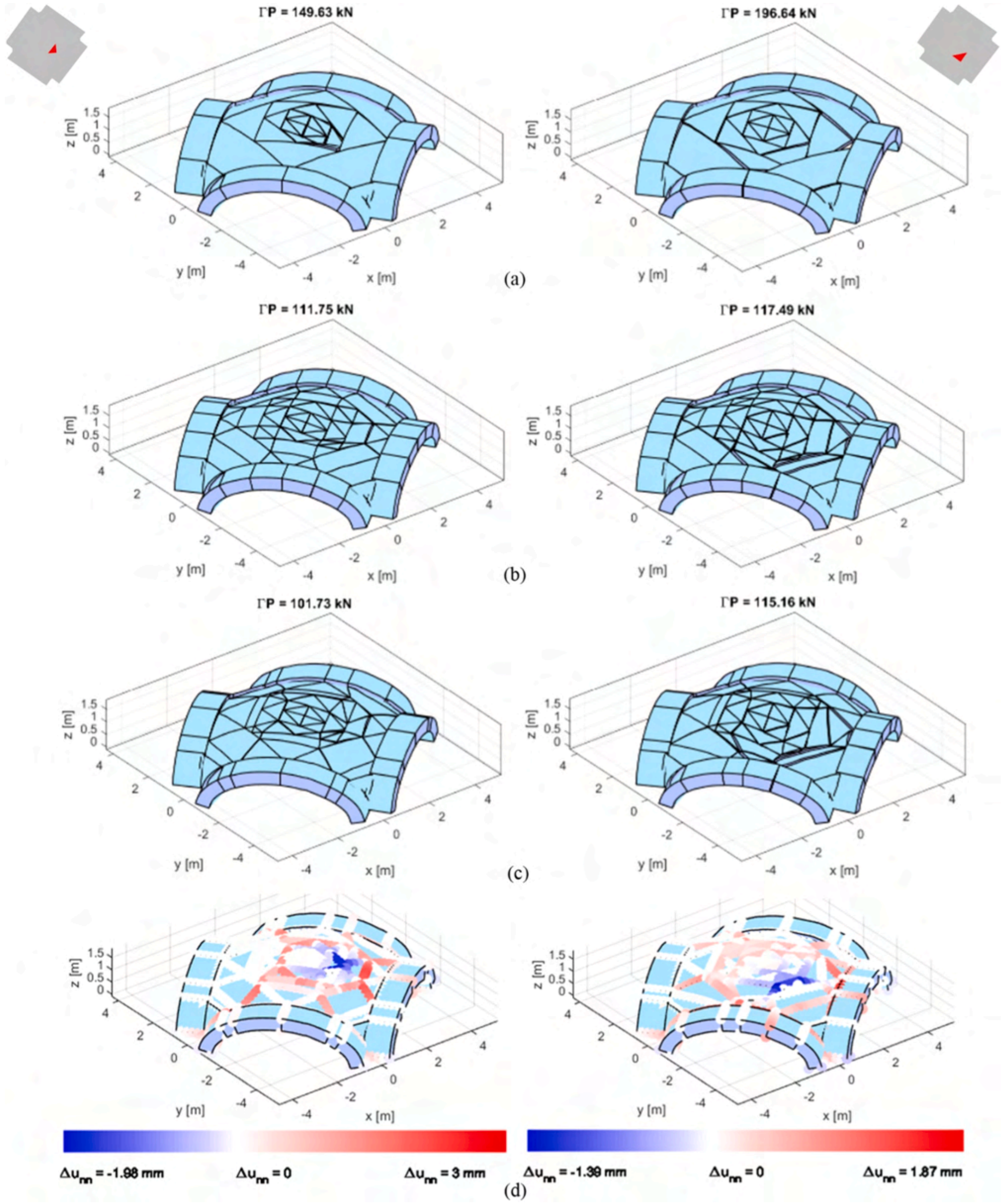

Fig. 16. Sail vaults under Load cases 3 (left) and 4 (right): (a-c) load-bearing capacity and collapse mechanisms in case of no mesh, initial and optimized mesh, (d) colormap representing the normal displacement jumps Δu_{nn} obtained by multiplying the velocity field by a unitary time factor (open crack lines in red, compression failures in blue, no damage in white).

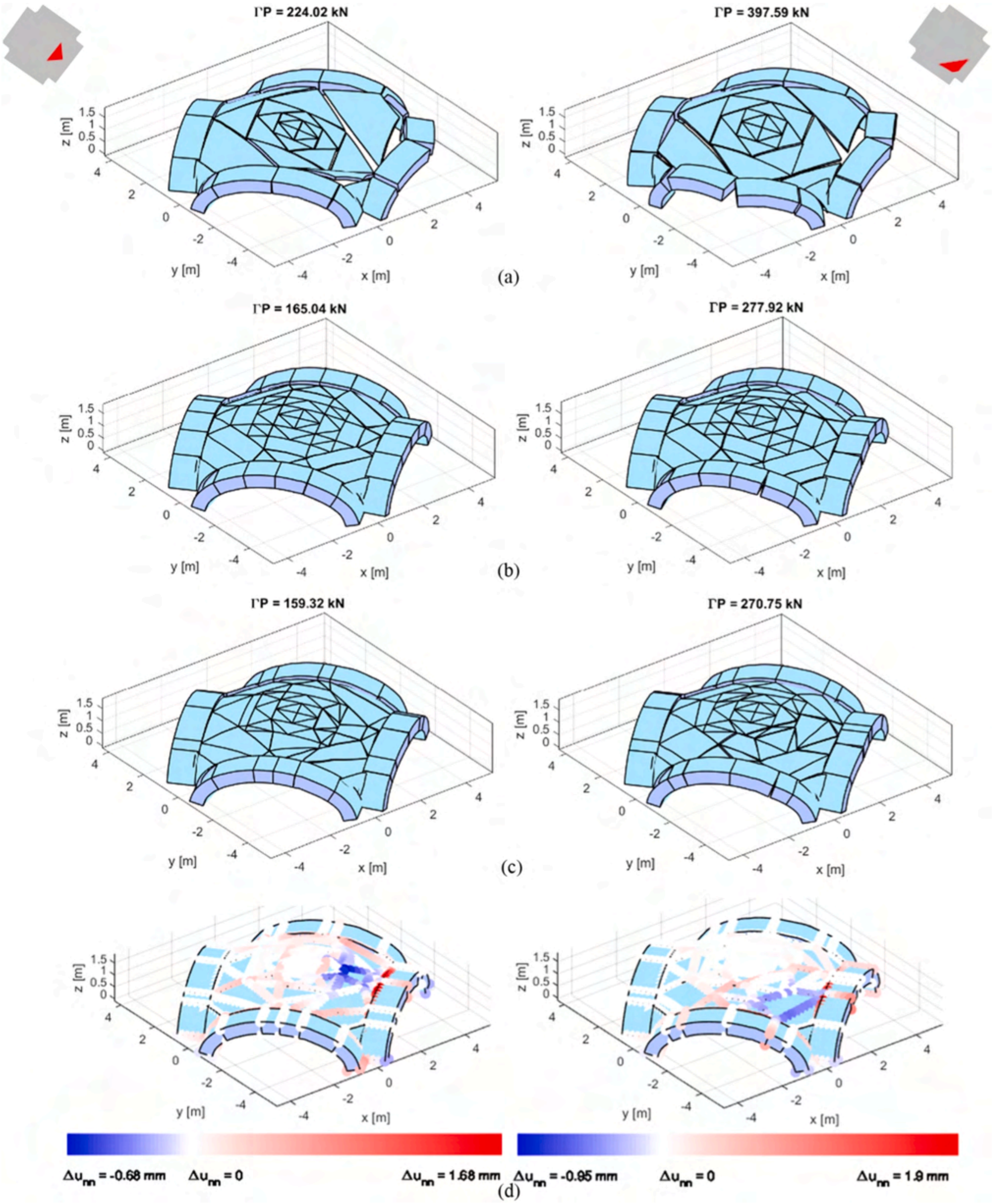

Fig. 17. Sail vaults under Load cases 5 (left) and 6 (right): (a-c) load-bearing capacity and collapse mechanisms in case of no mesh, initial and optimized mesh, (d) colormap representing the normal displacement jumps Δu_{nn} obtained by multiplying the velocity field by a unitary time factor (open crack lines in red, compression failures in blue, no damage in white).

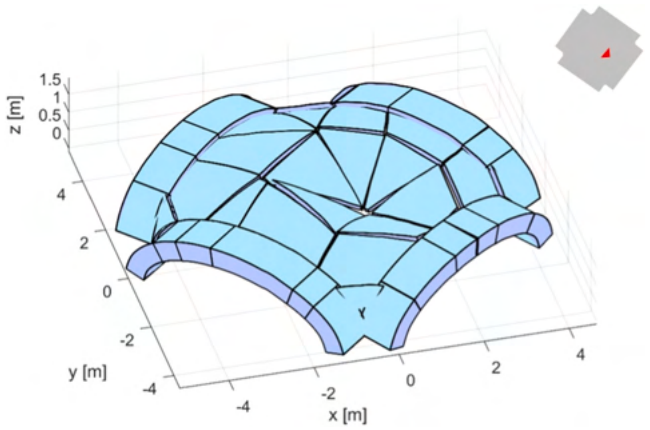

Fig. 18. Analysis of the sail vault assuming isotropic strength domain: collapse mechanism under Load case 3.

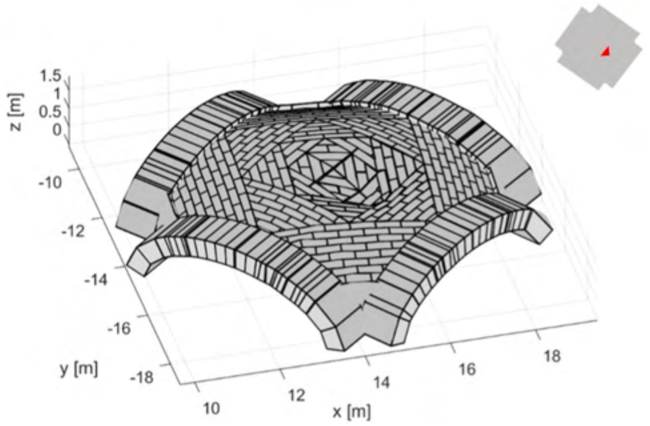

Fig. 19. Heterogeneous limit analysis of the sail vault: collapse mechanism under Load case 3.

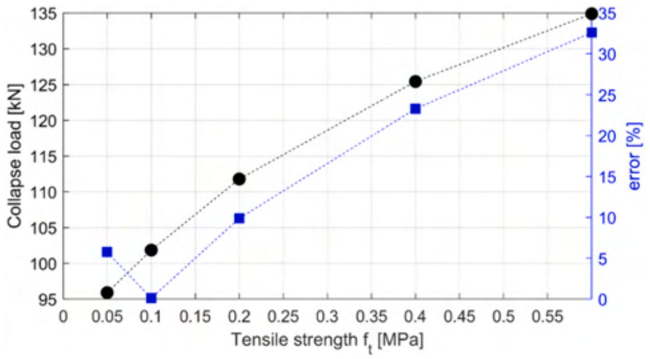

Fig. 20. Analysis of the sail vault under Load case 3: collapse load assuming isotropic strength domain and variable tensile strength and errors on the collapse load with respect to the orthotropic solution (errors reported in absolute value).

condition (expressed in terms of stresses along the boundaries) has been defined. The degrees of freedom of each brick are the two in-plane translations and the rotation about the same plane. Periodicity conditions should be imposed on the velocity field; however, in this model such conditions are implicitly taken into account once an equilibrated stress configuration is applied. Therefore, periodic constraint equations have not been manually included in this case, differently, for instance, from cases where a more complex REV is required [38].

The load conditions consist of distributions of stress directed along any direction θ. The related Cauchy stress tensor $\mathbf{\Sigma}$ is thus expressed as follows:

$$\mathbf{\Sigma} = \begin{bmatrix} \sigma_{11} & \sigma_{12} \\ \sigma_{12} & \sigma_{22} \end{bmatrix}, \text{ where } \begin{cases} \sigma_{11} = f_{\mathrm{tm}}\cos\theta \\ \sigma_{12} = \alpha c_{\mathrm{m}}, \alpha \in [0,1] \\ \sigma_{22} = f_{\mathrm{tm}}\sin\theta \end{cases} \tag{20}$$

where each component is defined as a function of the mortar resistance parameters. Note that a parameter α has been introduced in the expression of σ_{12}, since σ_{12} is not affected by the orientation θ. It is here specified that both α and θ are a-priori assigned as pre-defined constant values. The stress vector for each external boundary of the REV is computed according to Cauchy's stress theorem:

$$\boldsymbol{\sigma}_{\partial\Omega} = \mathbf{\Sigma}\boldsymbol{\eta}_{\partial\Omega} \tag{21}$$

in which $\boldsymbol{\eta}_{\partial\Omega}$ is the normal unit vector for the external boundary of the REV, see Fig. 7.

It is now useful to distinguish the normal and the shear components of the stress tensor into two separated stress tensors, respectively $\mathbf{\Sigma}_1$ and $\mathbf{\Sigma}_0$:

$$\mathbf{\Sigma} = \mathbf{\Sigma}_1 + \mathbf{\Sigma}_0, \text{where} \mathbf{\Sigma}_1 = \begin{bmatrix} \sigma_{11} & 0 \\ 0 & \sigma_{22} \end{bmatrix} \text{ and } \mathbf{\Sigma}_0 = \begin{bmatrix} 0 & \sigma_{12} \\ \sigma_{12} & 0 \end{bmatrix} \tag{22}$$

As previously mentioned, only $\mathbf{\Sigma}_1$ depends on the angle θ. Under this load condition, an upper bound limit analysis problem can be written. Here the external power is associated with stress along the boundary and can be defined as follows:

$$P_{ext,\partial\Omega} = \int_{\partial\Omega} \boldsymbol{\sigma}^T_{\partial\Omega} \dot{\mathbf{u}}_{\partial\Omega} d\partial\Omega = \int_{\partial\Omega} \boldsymbol{\sigma}^T_{\partial\Omega,0} \dot{\mathbf{u}}_{\partial\Omega} d\partial\Omega + \int_{\partial\Omega} \boldsymbol{\sigma}^T_{\partial\Omega,1} \dot{\mathbf{u}}_{\partial\Omega} d\partial\Omega \tag{23}$$

where $\boldsymbol{\sigma}_{\partial\Omega,1}$ and $\boldsymbol{\sigma}_{\partial\Omega,0}$ are obtained by applying Eq. (21) to the two stress tensors $\mathbf{\Sigma}_1$ and $\mathbf{\Sigma}_0$ respectively. In particular, the external power associated with the normal stress components is considered as a live load power, thus affected by an implicit load multiplier (let us call it Γ_f) that will coincide with the value of the objective function in the limit analysis problem, whereas the external power associated with the shear stress is maintained constant. Compatibility constraints are written to impose the associated flow rule along the interfaces, analogously to what was described in the previous section. Under these assumptions, the following LP problem is obtained:

$$\min \Gamma_f = \sum_{h=1}^{N_{\mathrm{int}}} \left(\sum_{e=1}^{Np} a_e \dot{\lambda}_e \bullet \mathbf{d}_{m,e} \right) - \int_{\partial\Omega} \boldsymbol{\sigma}_{\partial\Omega,0} \bullet \dot{\mathbf{u}}_{\partial\Omega} d\partial\Omega \text{ such that} \begin{cases} \boldsymbol{\sigma}_{\partial\Omega} = \mathbf{\Sigma}\boldsymbol{\eta}_{\partial\Omega} \\ \mathbf{A}_{comp}\left[\dot{\mathbf{u}}, \dot{\boldsymbol{\lambda}}\right] = \mathbf{0} \\ \int_{\partial\Omega} \boldsymbol{\sigma}_{\partial\Omega,1} \bullet \dot{\mathbf{u}}_{\partial\Omega} d\partial\Omega = 1 \\ \dot{\boldsymbol{\lambda}} \geq \mathbf{0} \end{cases} \tag{24}$$

Some observations are needed. First, it is observed that Eq. (24) still follows an upper bound formulation, but lower bound models can also be used, see [37]. Secondly, since both α and θ are constants, Eq. (24) provides a load multiplier that, once multiplied by the normal stress tensor, allows to obtain the amount of normal stress directed along the pre-assigned direction θ that, in the presence of a pre-assigned shear stress equals to αc_{m}, leads to the collapse of the REV. In other words, since a positive normal stress defined in agreement with Eq. (20) corresponds to a tensile stress oriented along θ, Eq. (24) allows to define the equivalent tensile strength $f_{t\theta}$ of the homogenized material along θ, under an assumed value of shear stress.

Alternatively, it can be stated that the outcome of Eq. (24) is a point with coordinates ($\sigma_{11} = \Gamma_f f_{\mathrm{tm}}\cos\theta$, $\sigma_{22} = \Gamma_f f_{\mathrm{tm}}\sin\theta$, $\sigma_{12} = \alpha c_{\mathrm{m}}$) that belongs to the homogenized failure surface.

The presented LP problem can be thus repeated for any θ within the

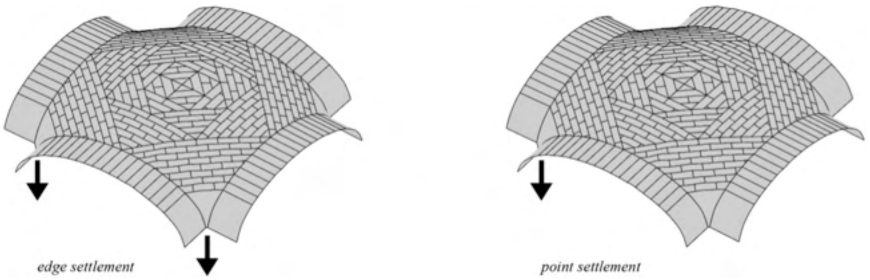

Fig. 21. Vertical settlements configurations considered in the analyses (each black arrow denotes an applied displacement of 10 mm).

interval [0, π/2] in order to obtain the homogenized tensile strength along all possible directions, again under a pre-assigned shear stress. With reference to the three-dimensional failure surface in the stress space $\sigma_{11}, \sigma_{22}, \sigma_{12}$, this allows to define a two-dimensional section of the surface corresponding to $\sigma_{12} = \alpha c_m$. By repeating the same analyses for several values of α within the interval [0,1], several two-dimensional sections of the homogenized failure surface can be obtained and consequently the three-dimensional surface is numerically quantified.

By using the described numerical procedure, the homogenized failure surface is here evaluated starting from the following resistance values for the mortar joints: $f_{tm} = 0.05$ MPa, $f_{cm} = 1$ MPa, $c_m = 1.4 f_{tm}$, and $\varphi_m = \pi/6$. It can be anticipated that the same values have been used in the numerical analyses of the vaults reported in the next section. The result obtained through the analysis of the REV is depicted in Fig. 8. The shape of the obtained surface is in good agreement with those analytically derived in [36], but its internal volume is limited through a higher number of planes because of the cut-off in tension. Each plane denotes a precise failure mode for the REV, including full tension and mixed tension-shear failures, which are also depicted in Fig. 8.

Therefore, the obtained homogenized failure surface can be used to numerically identify the tensile strength along any orientation. In particular, by evaluating the resistance values along the two main directions, a failure surface $f_\theta(\boldsymbol{\sigma})$ can be derived via Eqs. (13)-(14) and used within the upper bound limit analysis tool described in the previous section. Concerning the application to the sail vaults in Cagliari, for any interface located within a triangular portion and oriented along θ the evaluation of the internal dissipated power, Eq. (17), is modified as follows:

$$P_{in} = \sum\nolimits_{h=1}^{N_{int}} \int_{A_h} \boldsymbol{\sigma}^T \dot{\lambda} \frac{\partial f_\theta}{\partial \boldsymbol{\sigma}} dA_h \tag{25}$$

whereas for each interface between two different triangular portions, i.e. at the intersection between two different orientations θ_i and θ_j of textures, the equation becomes:

$$P_{in} = \sum\nolimits_{h=1}^{N_{int}} \int_{A_h} \boldsymbol{\sigma}^T \dot{\lambda} \frac{\partial \left(f_{\theta i} \cap f_{\theta j} \right)}{\partial \boldsymbol{\sigma}} dA_h \tag{26}$$

in which $f_{\theta i} \cap f_{\theta j}$ represents the Boolean intersection between the homogenized failure surfaces associated to the two orientations.

Some concluding remarks and observations are finally reported. As a first observation, the presented model hypothesizes infinitely resistant bricks, so the collapse behavior remains fully governed by the resistance and the geometric distribution of mortar joints. In future research, more complex models capable of considering the diffusion of cracks within bricks can be studied. Secondly, the REV here remains planar, thus it can be applied provided that the size of bricks is almost negligible in comparison to the radius of curvature of the vault, as in this case (otherwise, the REV should maintain the curvature of the actual structure, as discussed in detail in [26]).

4. Numerical results

4.1. Sail vaults in Cagliari, Italy

Specific attention is paid here to typical masonry sail vaults that were built in Cagliari (Sardinia, Italy) during the second half of the 19th century. Many of these vaults can be found on the ground floor of historic buildings in the city center, exhibiting the same peculiarities. In the case of a classic sail vault, the shape is obtained by intersecting a spherical cap with a prism that has a square base. In this case, the vaults have a rather shallow, lowered shape, that is almost flat at the crown. The defining feature of these vaults is the variation in the orientation of the masonry texture, see Fig. 1. Although there are no discontinuities in the curvature of the vaults across their entire surfaces, some triangular portions can be identified, see Fig. 9. Each of these is characterized by a different orientation of the masonry texture, with bed joints perpendicular to the bisector of each triangle. A minimum of four different textures can be observed, extending from the corners to the middle of the external arches, with more textures evident in the more refined case (Fig. 9). This arrangement of bricks could be related to the construction techniques adopted by masons, which may have allowed them to be built without formwork [1]. This hypothesis was recently investigated in [47], where an analysis of the construction stages of such vaults has been performed. These vaults are typically built by a single bricklayer using a running bond arrangement. They are made with typical Piedmont bricks from the late 19th century (with dimensions: length $l_b = 25$ cm, width $w_b = 12$ cm, and height $h_b = 6$ cm), resulting in a thickness of around 12 cm across the entire surface. In the pendentives, a head bond pattern is adopted up to an angle of around 30° from the springing.

The vaults rely on four external arches with a thickness of at least one whole brick, i.e. 25 cm. However, observations of the intrados do not clearly indicate whether the arch thickness remains constant along the arch's longitudinal direction. Even though lowered sail vaults with different brick patterns are widespread in southern Sardinia, particularly in the Cagliari area, only preliminary studies of their structural behavior have been carried out to date, [48–49]. A series of photogrammetric surveys were performed to investigate the vault effective geometry at both the macro level (vault shape) and the micro level (brick patterns). Fig. 9 shows the obtained geometrical outlines, along with the main dimensions of the analyzed vault. The vault is nearly square, with sides measuring 5.88 m and 5.68 m, respectively. The average rise of the lateral arches is approximately 1.48 m, while the crown height at the top of the vault is about 1.80 m.

4.2. Model description

The analysis of a single vault is here reported. Starting from the result of the laser scanner survey, a series of horizontal and vertical sections of a single vault has been extracted and imported in the modeling software Rhinoceros. Here, an assembly of NURBS surfaces has been created, which describes the surface of the vault with a very good approximation. The sections and the NURBS model are depicted in Fig. 10.

It is important to observe that a different NURBS surface has been

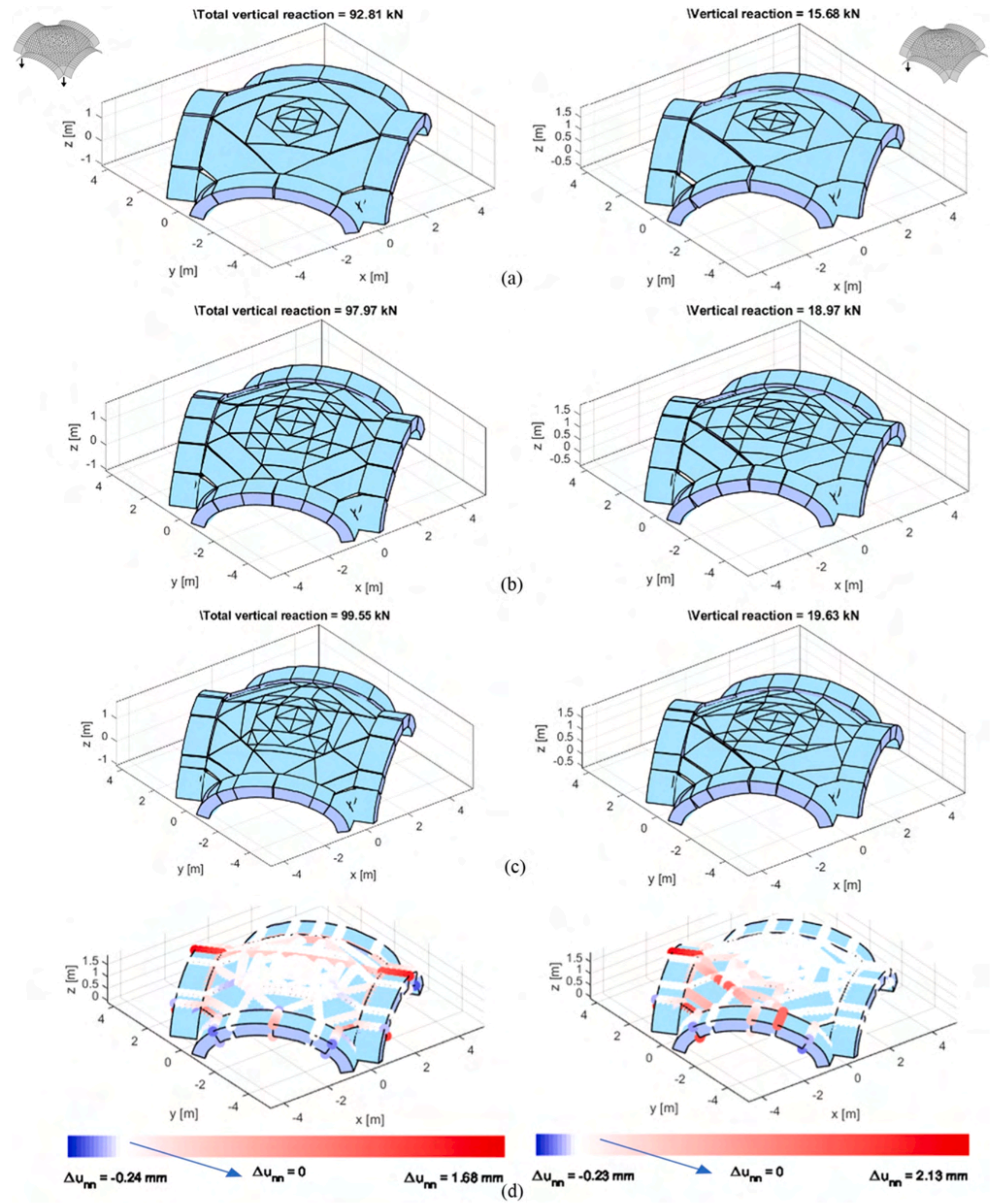

Fig. 22. Sail vaults under edge settlement (left) and point settlement (right): (a-c) reaction forces and collapse mechanisms in case of no mesh, initial and optimized mesh (displacements scaled by 100), (d) colormap representing the normal displacement jumps Δu_{nn} (open crack lines in red, compression failures in blue, no damage in white).

adopted to represent each triangular portion of the vault, which is characterized by a specific texture orientation. This choice facilitates the application of the orthotropic model within the limit analysis tool, as it will be described later. Moreover, the changes in the texture orientation are automatically identified as common edges between the adjacent NURBS surfaces in the initial model.

In all the following analyses the vault is assumed to be constrained along the external edges and at the base. To better reproduce the constraint along the external edges, four arches have been modeled along the perimeter. Without more detailed information regarding the extrados of the vault, the thickness of these arches has been supposed to be 30 cm. The so-defined NURBS model of the sail vault is depicted in Fig. 11a, whereas Fig. 11b shows the indexes assigned to each initial NURBS surface (Fig. 11b just provides a useful reference for the next simulations).

By using the numerical procedures presented in Section 3, the vault is studied under vertical load and differential settlements. The initial mesh has been defined by subdividing each triangular portion through a set of lines, which represent potential cracks propagating within the element, see Fig. 12a.

Each subdivision line starts from a node on one edge and ends on another node belonging to one of the opposite edges, where the position of each node on the edge is determined by a numerical variable t_i within the range (0, 1). Only the smallest triangular elements located at the top of the vault have been left unmeshed in order to maintain uniform the elements size in the model. The initial position of the subdivision lines, which is assigned through a starting value for each variable t_i, has been defined by taking into account the structural behavior of the sail vault under vertical load and the orientation of the masonry textures: a schematization of the mesh for the single triangular portion is depicted in Fig. 12a. The initial mesh depicted in Fig. 12b is obtained setting $t_i = 0.5$ for all the lines. When one of these variables is changed the corresponding node moves along the edge, reorienting the subdivision line and altering the mesh. Thus, the mesh adaptation performed via GA will include 24 variables. Since the model derives directly from the laser scanner survey and accounts for all geometric imperfections with respect to a perfectly shaped vault, no symmetry conditions have been applied in the position of such subdivision lines, thus avoiding any pre-assumed symmetric collapse mechanism. With 24 variables in total, populations of 100 individuals and 200 generations have been adopted in the GA-mesh adaptation for all next simulations.

The ultimate resistance values assigned to each potential fracture line take into account the actual texture orientation along that line. This is performed according to Eqs. (13)–14), once the orientation of the line with respect to the two main directions of the specific NURBS surface (which coincide with the main directions of the local texture) has been identified. In Figure 13a, the two main directions for a single NURBS surface are depicted: direction 1, parallel to the bed joints of the corresponding triangular portion, and direction 2, orthogonal to the first one. A different set of masonry properties for each direction [47] has been determined by analyzing the REV as described in Section 4: the obtained values are reported in Table 1. It is expected that the lines located along the changes in the texture orientation (corresponding to the edges of the initial surfaces) will exhibit weaker resistance properties, consequently becoming crucial in the development of the collapse mechanism.

In all following analyses, the load multiplier has been evaluated on three configurations: the unmeshed model, the model with initial mesh (meaning that, in this case, all variables t_i remain equal to 0.5), and finally the model with optimized mesh that derives from mesh adaptation. The scope is to observe directly how the position of fracture lines, which are internal to the triangular portions, affect the load-bearing capacity for this typology of vault, considering the orthotropic properties of each portion, with respect to the lines of texture changes.

4.3. *Analyses under vertical loads*

Several configurations of vertical load have been studied, see Fig. 14. In the first one, the vault is loaded at the extrados through a distributed uniform vertical load, whose reference value is 1 kN/m^2. The second and third sets of simulations include a point load at the top and uniform loads distributed only along one of the initial triangular portions. Results are shown in Fig. 15 to Fig. 17 for the three configurations. In Fig. 15, the analyses under uniform vertical load (Load case 1) and point load at the top (Load case 2) are shown. Under uniform load, the additional fracture lines are crucial for identifying the load-bearing capacity, which decreases from 16.47 kN/m^2 for the initial regular discretization to 13.62 kN/m^2 for the optimized case. It can be observed that crushing assumes a fundamental role in comparison with tensile and shear failures; this is not unexpected for a shallow (i.e. lowered) shape vault. Under the application of a point load, the collapse involves a limited part at the top of the vault and takes place starting from the changes of texture. Additional fracture lines seem unnecessary in this case, the load bearing capacity remains around 124 kN.

In Fig. 16 and Fig. 17, Load cases 3, 4, 5 and 6 are applied, thus obtaining collapse mechanisms less symmetric and more difficult to predict. It is observed that the peak load decreases much more between unmeshed and initial mesh model than between initial mesh and optimized model. It can be deduced that the fracture lines corresponding to the changes of textures are not sufficient to represent the collapse mechanism, whereas the initial mesh selected is already quite close to the exact configuration of the cracks.

4.4. *Comparison with isotropic model*

In order to assess the significance of the orthotropy, an additional analysis was performed by assuming isotropic strength domain. In this case, a new model of the vault was developed by disregarding the texture variations, meaning that the sail vault has been modelled as a single continuous surface rather than subdividing it into triangular portions. The model was analyzed under Load case 3 (Fig. 16, left). By assuming isotropic properties, a simple Mohr-Coulomb strength domain has been applied to all the interfaces, independently of their orientation. Two isotropic domains have been separately considered, incorporating respectively the resistance along the staggered direction of the blocks (corresponding to direction 1, see Table 1) and of the head joints only (direction 2), thus resulting in two additional simulations. As an exception, the perimetral arches were always assigned the bed joints properties, since cracks here are supposed to occur along the bed joints orientation. The obtained collapse mechanism is the same for both the isotropic configurations and is depicted in Fig. 18 (without the initial subdivision into triangular portions, an initial mesh of 4 ×4 elements has been used for the sail). The corresponding collapse loads were equal to 94.61 kN and 104.39 kN respectively for the two cases, whereas the result obtained in presence of orthotropy (101.73 kN, see Fig. 16c) stands between the two values. This outcome is consistent with the expectations, since the two main directions are associated with the lowest and the highest internal dissipation in the kinematic limit analysis model. It is worth noting that, in the orthotropic formulation, any interface oriented along an intermediate direction is characterized by an amount of internal dissipation between these bounds, in accordance with the adopted elliptical interpolation law (see Eqs. (13–14), where the right-hand-side terms of Eq. (13) are directly used into Eq. (17)).

From such results, it can be stated that assuming an isotropic strength domain with bed joints failure properties provides a result that is conservative from the point of view of the collapse load but does not reproduce realistically the failure mechanism, since the contribution of orthotropy is neglected. In contrast, using an orthotropic model provides a more physically consistent description of the vault's collapse behaviour. The latter point is confirmed by comparing the result obtained with the orthotropic model to the one obtained via heterogeneous limit analysis, which shows a very good agreement in terms of failure mechanism, see Fig. 19 (note that the total number of elements has been reduced by using larger blocks with the same aspect ratio, i.e. preserving the running bond texture: this allows to keep the computational effort manageable but increases the collapse load that results equal to 105.53 kN).

Finally, it is worth mentioning that the differences found in the load carrying capacity are roughly around 5 %. Such an outcome is mainly due to the small value of tensile strength assumed, and to the fact that quasi no-tension vaults tend to carry external loads thanks to their shape. Fig. 20 shows the results obtained in terms of collapse load for the same example where tensile strength is assumed 2, 4, 8 and 12 times the original one (f_{tm}=0.05 MPa) — and keeping all the other mechanical parameters unchanged. In the same figure, the corresponding errors on the failure load, taking the orthotropic solution as reference, are also represented. As can be seen and as expected, an increase of the tensile strength reflects in errors of the prediction of the load carrying capacity that may become relevant from an engineering perspective.

4.5. Analyses under differential base settlements

Finally, the vault has been analyzed under differential vertical settlements, in particular a line settlement involving two supports and a localized one applied to one support only, see Fig. 21. In both cases, the applied displacements are equal to 10 mm. The final crack pattern and the deformed structure are depicted in Fig. 22. It is easy to observe that the perimeter arches show the typical behavior of arches subjected to settlements, whereas the vault follows the arch mechanisms.

Note that the reaction forces increase when the mesh is optimized. This outcome is correct, as the minimization is applied to the work done by the reaction forces: when the displacement is constant and the work is negative, its minimization is equivalent to maximizing the reaction force. Finally, it is also worth noting that the highest relative displacements have been found along the texture changes.

5. Conclusions

The paper has presented a fast and robust two-step approach for the analysis of double curvature masonry vaults which exhibit a twofold complexity, one related to the overall geometry and the other to the building technology used, that in some cases relies in the tessellation of different portions of the vault with bricks disposed – portion by portion – in different preferential directions. Heterogeneous methods of analysis proved to be unpractical in the meshing phase, slow in the prediction of the ultimate load carrying capacity when limit analysis computations or Distinct Element Method are applied, sometimes failing in finding a converged solution because of the many kinematic variables involved. The study here proposed overcomes all such problems, being characterized by a two-step procedure that combines in series (i) homogenization performed in the rigid plastic range to retrieve the orthotropic strength domain and (ii) adaptive limit analysis (or LP analyses in presence of applied displacements) with few NURBS elements. A discretization brick by brick is thus avoided thanks to homogenization, whereas rigid-plastic analyses at the macro-scale – i.e. on the entire vault – can be carried out with very few elements, exploiting the adaptation features of NURBS.

The proposed procedure is aimed at putting at disposal of interested practitioners a simple assessment tool which does not require excessive computational efforts and realistically predicts masonry behavior. Indeed such behavior is not characterized by meaningful elastic deformability (i.e. displacements are mainly concentrated on cracks, and the vault carries external loads only thanks to its shape). Future developments will be the integration of the adaptive software in a standard FE code to study the seismic behavior of clusters of vaults inside existing buildings and the implementation of strengthening elements (e.g. tie rods) to evaluate the vulnerability reduction in presence of already cracked vaults, due to active settlements.

CRediT authorship contribution statement

Nicola Grillanda: Writing – review & editing, Writing – original draft, Software, Methodology, Investigation, Formal analysis. **Emanuele Reccia:** Writing – review & editing, Writing – original draft, Validation, Supervision, Methodology, Conceptualization. **Valentina Pintus:** Resources, Investigation, Data curation. **Antonio Cazzani:** Supervision, Funding acquisition. **Gabriele Milani:** Writing – review & editing, Writing – original draft, Validation, Supervision, Methodology, Conceptualization.

Declaration of Competing Interest

The authors declare that they have no known competing financial interests or personal relationships that could have appeared to influence the work reported in this paper.

Acknowledgments

The author(s) disclosed receipt of the following financial support for the research, authorship, and/or publication of this article: The financial support of Fondazione di Sardegna through grant “Surveying, modelling, monitoring and rehabilitation of masonry vaults and domes”, i.e., Rilievo, modellazione, monitoraggio e risanamento di volte e cupole in muratura (RMMR) (CUP code: F72F20000320007) is grateful acknowledged.

Data availability

No data was used for the research described in the article.

References

[1] Wendland D. Traditional vault construction without formwork: masonry pattern and vault shape in the historical technical literature and in experimental studies. Int J Archit Herit 2007;1(4):311–65.
[2] Bertolesi E, Adam JM, Rinaudo P, Calderón PA. Research and practice on masonry cross vaults–A review. Eng Struct 2019;180:67–88.
[3] Roca P, Cervera M, Pelà L, Clemente R, Chiumenti M. Continuum FE models for the analysis of Mallorca Cathedral. Eng Struct 2013;46:653–70.
[4] Atamturktur S, Bornn L, Hemez F. Vibration characteristics of vaulted masonry monuments undergoing differential support settlement. S Eng Struct 2011;33(9):2472–84.
[5] Compán V, Pachón P, Cámara M, Lourenço PB, Sáez A. Structural safety assessment of geometrically complex masonry vaults by non-linear analysis. The Chapel of the Würzburg Residence (Germany). Eng Struct 2017;140:1–13.
[6] Brune Ph, Perucchio R. Roman concrete vaulting in the great hall of Trajan's markets: Structural evaluation. ASCE J Archit Eng 2012;18(4):332–40.
[7] Mercuri M, Pathirage M, Gregori A, Cusatis G. Masonry vaulted structures under spreading supports: Analyses of fracturing behavior and size effect. J Build Eng 2022;45:103396.
[8] Cattari S, Resemini S, Lagomarsino S. Modelling of vaults as equivalent diaphragms in 3D seismic analysis of masonry buildings. Struct Anal Hist Constr Preserv Saf Significance Proc 6th Int Conf Struct Anal Hist Constr SAHC08 2008;1:517–24.
[9] Alforno M, Venuti F, Monaco A, Calderini C. Seismic behaviour of cross vaults with different brick pattern. Bull Earthq Eng 2022;20(8):3921–39.
[10] Gaetani A, Bianchini N, Lourenço PB. Simplified micro-modelling of masonry cross vaults: Stereotomy and interface issues. Int J Mason Res Innov 2021;6(1):97–125.
[11] Paris V, Pizzigoni A, Adriaenssens S. Statics of self-balancing masonry domes constructed with a cross-herringbone spiraling pattern. Eng Struct 2020;215:110440.
[12] Pourfouladi M, Pingaro N, Valente M. PoliBrick plugin as a parametric tool for digital stereotomy modelling. Comput Struct 2025;311:107722.
[13] Mercuri M, Pathirage M, Gregori A, Cusatis G. Influence of self-weight on size effect of quasi-brittle materials: Generalized analytical formulation and application to the failure of irregular masonry arches. Int J Fract 2024;246(2-3):117–44.
[14] Roca P, López-Almansa F, Miquel J, Hanganu A. Limit analysis of reinforced masonry vaults. Eng Struct 2007;29(3):431–9.
[15] Gago AS, Alfaiate J, Lamas A. The effect of the infill in arched structures: Analytical and numerical modelling. Eng Struct 2011;33(5):1450–8.
[16] Heyman J. The stone skeleton. Int J Solids Struct 1966;2(2):249–56.
[17] Heyman J. The safety of masonry arches. Int J Mech Sci 1969;11(4):363–82.

[18] Heyman J. On shell solutions for masonry domes. Int J Solids Struct 1967;3(2):227–41.
[19] Como M. Statics of historic masonry constructions. Berlin, Heidelberg: Springer; 2013.
[20] Cavicchi A, Gambarotta L. Lower bound limit analysis of masonry bridges including arch-fill interaction. Eng Struct 2007;29(11):3002–14.
[21] Cavicchi A, Gambarotta L. Collapse analysis of masonry bridges taking into account arch-fill interaction. Eng Struct 2005;27(4):605–15.
[22] Angelillo M. The model of Heyman and the statical and kinematical problems for masonry structures. Int J Mason Res Innov 2019;4(1-2):14–21.
[23] Marmo F, Masi D, Mase D, Rosati L. Thrust network analysis of masonry vaults. Int J Mason Res Innov 2019;4(1-2):64–77.
[24] Fraddosio A, Lepore N, Piccioni MD. Thrust Surface Method: An innovative approach for the three-dimensional lower bound Limit Analysis of masonry vaults. Eng Struct 2020;202:109846.
[25] Nodargi NA, Bisegna P. Generalized thrust network analysis for the safety assessment of vaulted masonry structures. Eng Struct 2022;270:114878.
[26] Milani E, Milani G, Tralli A. Limit analysis of masonry vaults by means of curved shell finite elements and homogenization. Int J Solids Struct 2008;45:5258–88.
[27] Tralli A, Chiozzi A, Grillanda N, Milani G. Masonry structures in the presence of foundation settlements and unilateral contact problems. Int J Solids Struct 2020;191–192:187–201.
[28] Iannuzzo A, Angelillo M, De Chiara E, De Guglielmo F, De Serio F, Ribera F, Gesualdo A. Modelling the cracks produced by settlements in masonry structures. Meccanica 2018;53(7):1857–73.
[29] Malena M, Angelillo M, Fortunato A, de Felice G, Mascolo I. Arch bridges subject to pier settlements: continuous vs. piecewise rigid displacement methods. Meccanica 2021;56(10):2487–505.
[30] Portioli F, Cascini L. Large displacement analysis of dry-jointed masonry structures subjected to settlements using rigid block modelling. Eng Struct 2017;148:485–96.
[31] Grillanda N, Chiozzi A, Milani G, Tralli A. NURBS solid modeling for the three-dimensional limit analysis of curved rigid block structures. Comput Methods Appl Mech Eng 2022;399:115304.
[32] D'Ayala DF, Tomasoni E. Three-dimensional analysis of masonry vaults using limit state analysis with finite friction. Int J Archit Herit 2011;5(2):140–71.
[33] Lengyel G. Discrete element analysis of gothic masonry vaults for self-weight and horizontal support displacement. Eng Struct 2017;148:195–209.
[34] Dell'Endice A, Iannuzzo A, DeJong MJ, Van Mele T, Block Ph. Modelling imperfections in unreinforced masonry structures: Discrete element simulations and scale model experiments of a pavilion vault. Eng Struct 2021;228:111499.
[35] Milani G, Rossi M, Calderini C, Lagomarsino S. Tilting plane tests on a small-scale masonry cross vault: Experimental results and numerical simulations through a heterogeneous approach. Eng Struct 2016;123:300–12.
[36] de Buhan P, de Felice G. A homogenization approach to the ultimate strength of brick masonry. J Mech Phys Solids 1997;45(7):1085–104.
[37] Milani G, Lourenço PB, Tralli A. Homogenised limit analysis of masonry walls, Part I: Failure surfaces. Comput Struct 2006;84:166–80.
[38] Tiberti S, Milani G. 2D pixel homogenized limit analysis of non-periodic masonry walls. Comput Struct 2019;219:16–57.
[39] Krabbenhøft K, Lyamin AV, Sloan SW. Three-dimensional Mohr-Coulomb limit analysis using semidefinite programming. Commun Numer Methods Eng 2008;24(11):1107–19.
[40] Krabbenhøft K, Lyamin AV, Sloan SW. Formulation and solution of some plasticity problems as conic programs. Int J Solids Struct 2007;44(5):1533–49.
[41] Portioli F, Casapulla C, Gilbert M, Cascini L. Limit analysis of 3D masonry block structures with non-associative frictional joints using cone programming. Comput Struct 2014;143:108–21.
[42] Chiozzi A, Milani G, Tralli A. A Genetic Algorithm NURBS-based new approach for fast kinematic limit analysis of masonry vaults. Comput Struct 2017;182:187–204.
[43] Piegl L, Tiller W. The NURBS book. Berlin: Springer; 1995.
[44] De Boor C. A practical guide to splines. New York: Springer; 1978.
[45] Grillanda N, Chiozzi A, Bondi F, Tralli A, Manconi F, Stochino F, Cazzani A. Numerical insights on the structural assessment of historical masonry stellar vaults: the case of Santa Maria del Monte in Cagliari. Contin Mech Thermodyn 2021;33:1–24.
[46] Haupt RL, Haupt SE. Practical genetic algorithms. New York: John Wiley & Sons; 1998.
[47] Zucca M, Reccia E, Stochino F, Cazzani A. On the construction stage analysis of historical masonry vaults. Int J Mason Res Innov 2024;9(5-6):451–74.
[48] Cazzani A, Grillanda N, Milani G, Pintus V, Reccia E. Structural evaluation of typical historical masonry vaults in Cagliari: sensitivity to brick arrangements, In Proceedings of. 12th Int Conf Struct Anal Hist Constr (SAHC 2021) 2021:2342–53.
[49] Cazzani A, Pintus V, Reccia E, Grillanda N, Milani G. Numerical insights on the structural assessment of typical historical masonry vaults of Cagliari, in Brick and Block Masonry – From Historical to Sustainable Masonry. Proc 17th Int Brick Block Mason Conf (IB2MaC2020) 2020:655–61.